Research Square

Preprints are preliminary reports that have not undergone peer review.
They should not be considered conclusive, used to inform clinical practice,
or referenced by the media as validated information.

A high-precision measurement method for ruby balls based on multi-scale adaptive edge detection

Wen Sun

WenSun372@outlook.com

Henan Geology Mineral College

Research Article

Keywords: Ruby ball measurement, multi-scale edge detection, dark field imaging, sub-pixel positioning, high-precision measurement

Posted Date: July 6th, 2026

DOI: https://doi.org/10.21203/rs.3.rs-9940710/v1

License: This work is licensed under a Creative Commons Attribution 4.0 International License.
Read Full License

Additional Declarations: No competing interests reported.

A high-precision measurement method for ruby balls based on multi-scale adaptive edge detection

Wen Sun *

Henan Geology Mineral College,Zhengzhou Henan,451464,China

* Corresponding author:Wen Sun,e-mail:WenSun372@outlook.com

Author Contributions

Wen Sun: Conceptualization, Methodology, Software, Validation, Formal analysis, Investigation, Resources, Data curation, Writing – original draft, Writing – review & editing, Visualization, Supervision, Project administration, Funding acquisition.

Conflict of Interest

The authors declare no competing interests.

Ethical Approval

This research did not involve human participants or animals requiring ethical approval.

Data Availability

The data supporting this study's findings are available from the corresponding author upon reasonable request.

Funding

No funding was received for conducting this study.

Clinical trial number

Not applicable.

Consent to Publish

All authors have reviewed the final version and consented to its publication.)

Consent to Participate

Not applicable.

Abstract: This paper proposes a high-precision measurement method for ruby balls based on multi-scale adaptive edge detection. By combining dark field imaging technology with improved Canny algorithm, the accuracy and robustness of edge extraction have been significantly improved. When measuring 5mm ruby balls, the average absolute error of this method is only 1.6μm, which is about 66% lower than the Hessian matrix method and about 83% lower than the regionprops method; When the signal-to-noise ratio drops to 20 dB, the

error growth only reaches 2.4m, while the traditional Canny algorithm reaches 6.5μm. For samples with different diameters (3-12mm) and materials (ruby, ceramic, hard alloy), the algorithm's measurement error is controlled within 0.2-0.3μm, and the repeatability is better than 0.15μm, meeting the micrometer level accuracy requirements of high-end manufacturing industry. The experiment verified the excellent adaptability and robustness of this method in complex environments.

Keywords: Ruby ball measurement, multi-scale edge detection, dark field imaging, sub-pixel positioning, high-precision measurement

1. Introduction

As the core component of precision measuring equipment and standard instruments, the micrometer level accuracy of the geometric dimensions of ruby balls directly affects the assembly accuracy and product reliability of high-end manufacturing industries [1]. In the fields of aerospace, precision instruments, and optical systems, non-contact high-precision measurement faces core challenges such as edge blurring caused by high reflective surfaces and low contrast imaging noise interference [2]. Traditional optical measurement methods often suffer from positioning deviations due to edge diffusion effects and noise sensitivity when dealing with strongly reflective and weakly textured targets such as ruby balls, making it difficult to meet sub micron measurement requirements [3]. With the development of computer vision and multi-scale analysis technology, the solution of integrating optical imaging optimization and intelligent edge detection has become an important direction to break through the measurement bottleneck, and there is an urgent need to develop innovative methods that balance robustness and accuracy.

In recent years, edge detection and sub-pixel localization technology have made significant progress in the field of precision measurement. Borkenstein et al. quantified the influence of material mechanical properties on measurement depth through nanoindentation technology, revealing the sub surface light scattering effect caused by the semi transparent nature of ruby balls, providing a theoretical basis for understanding the mechanism of edge blurring [4]. The dynamic diamond anvil cell system developed by Jin et al. achieved microsphere compression

rate monitoring in extreme environments, and its multi-scale signal processing framework effectively suppressed thermal noise interference, but did not solve the problem of high reflection imaging in the visible light band [5]. Renner et al. optimized the contrast of material surface imaging by precisely controlling the ratio of red light/far red light, and confirmed that adaptive lighting strategy can improve the edge signal-to-noise ratio. However, this method lacks adaptability to complex curved targets [6]. Linsler et al. analyzed the microstructure evolution of the sub surface layer of iron crystals based on scratch testing, and pointed out the localization limitations of traditional Canny algorithm in gradient mutation areas, providing micro mechanical insights for edge continuity optimization [7]. Although these studies have made breakthroughs in material property analysis, noise suppression, and optical control, they have not systematically solved the collaborative optimization problems of edge weakening, noise sensitivity, and multi-scale feature fusion of high reflection spheres in dark field imaging.

The current high-precision measurement of ruby balls faces three technical bottlenecks: Firstly, fixed scale edge detection algorithms are difficult to balance the contradiction between noise suppression and detail preservation. Large scale smoothing leads to weak edge loss, while small-scale processing amplifies imaging noise [8]; Secondly, the global threshold strategy cannot adapt to the local contrast fluctuations caused by uneven lighting in dark field imaging, resulting in edge breakage or pseudo edge proliferation [9-10]; Thirdly, the existing circle fitting methods have insufficient sensitivity to the spatial distribution of sub-pixel edge points, and are easily affected by outliers under strong noise interference, resulting in fitting deviation [11]. Especially for ruby balls with a diameter less than 5 mm, the problem of confusion between their edge diffraction rings and the true contour has not been effectively resolved. These defects result in insufficient measurement stability of traditional methods in complex industrial environments, making it difficult to meet the requirements of micrometer level repeatability.

This paper proposes a high-precision measurement framework for ruby balls using multi-scale adaptive edge detection. To address the challenge of scale selection, a Gaussian kernel scale space collaborative mechanism is designed to fuse multi-scale edge responses through gradient direction consistency weighted fusion, balancing noise robustness and detail

resolution [12-13]; Innovate a dynamic threshold model driven by local information entropy, combining sub region statistical features with bilinear interpolation smoothing to achieve edge continuity optimization under uneven lighting conditions; Develop a cubic spline sub-pixel localization and geometric distance least squares fitting algorithm based on RANSAC screening to effectively suppress outlier interference [14]. The experimental system integrates a dark field imaging optical path and a 12 bit high dynamic range camera, and regulates the scattering angle distribution through a circular LED light source to provide high contrast raw images for the algorithm. The validation plan covers different materials (ruby/ceramic/hard alloy), diameters (3-12 mm), and noise environments, comprehensively evaluating the universality and reliability of the method in industrial scenarios [15].

2. Measurement system and experimental setup

Ruby balls are widely used in high-precision measurements due to their high hardness, low thermal expansion, and resistance to deformation. In order to achieve high-precision non-contact measurement, this paper used dark field imaging technology, which uses a special optical path to prevent direct light that has not been scattered or diffracted from entering the imaging system, only receiving scattered light from the edge of the ruby sphere, forming a high contrast contour [16]. The system adopts a circular LED light source at an angle of 15° to the optical axis, with a distance of about 150mm, and is equipped with a 12 bit high dynamic range industrial camera and a telephoto lens, effectively reducing perspective distortion, as shown in Figure 1. The mathematical model of its scattered light intensity is as follows (1):

$$I(\theta)=I_0 \cdot P(\theta) \cdot \sin^2(\theta) \quad (1)$$

Among them, I_o represents the intensity of incident light, θ is the scattering angle, $P(\theta)$ is the scattering phase function, describing the distribution of scattering intensity of light at different angles.

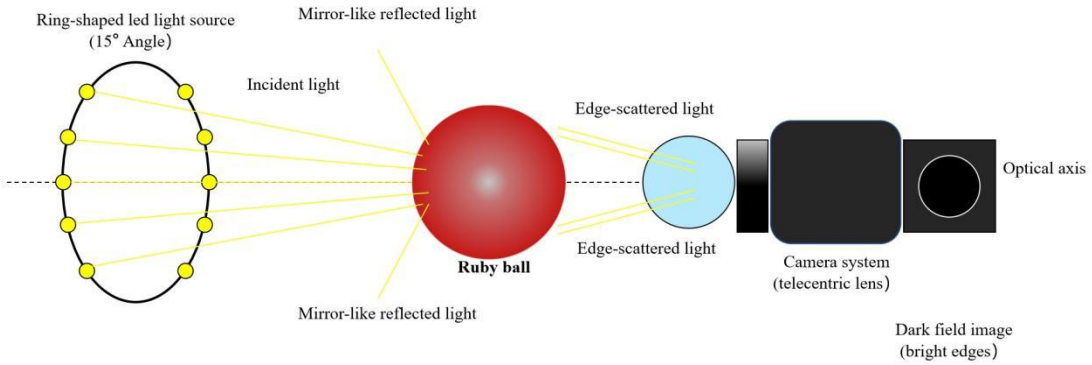


Figure 1 Schematic diagram of ruby ball dark field imaging principle

3. Multi scale adaptive edge detection algorithm

3.1 One time edge detection: improving Canny operator

Based on multi-scale Gaussian kernel smoothing and adaptive threshold determination method, this paper constructed an improved Canny edge detection algorithm complete process for high-precision measurement of ruby balls. The entire algorithm process mainly includes core steps such as image preprocessing, multi-scale analysis, gradient calculation, non maximum suppression, adaptive threshold determination, and edge tracking. The flowchart is shown in Figure 2.

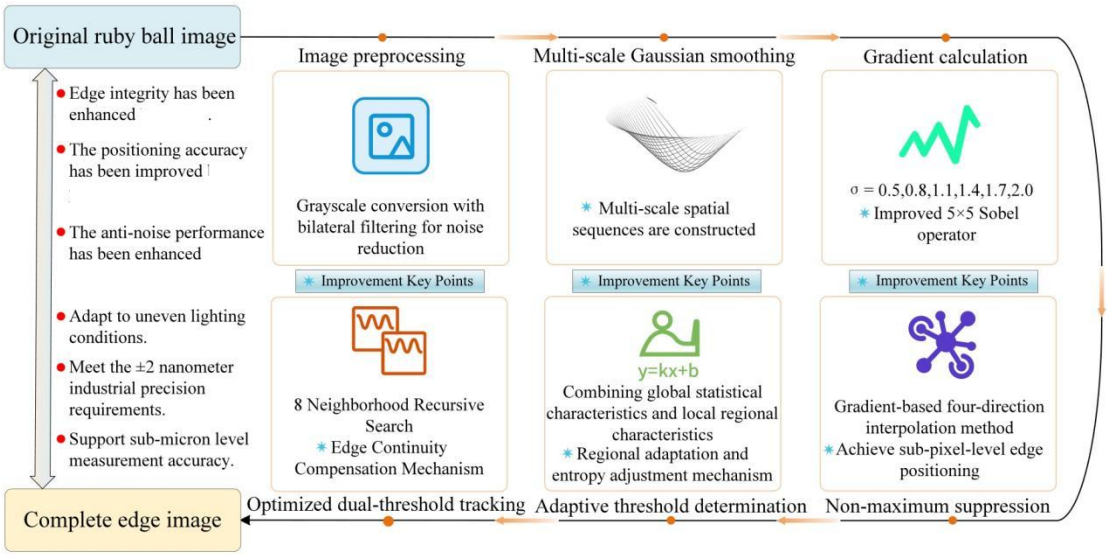


Figure 2 Flow Chart of Improved Canny Edge Detection Algorithm

Although the traditional Canny edge detection algorithm is widely used, it often faces problems of noise interference and edge loss when processing industrial component images

with high reflectivity and blurred edges, such as ruby balls. In order to solve this problem, this paper proposes a multi-scale Gaussian kernel smoothing method, which improves the robustness and accuracy of edge detection by analyzing image features in different scale spaces [17].

Multi scale Gaussian kernel smoothing is based on scale space theory, which suggests that targets in real images exist in different scale spaces. By applying Gaussian filters with different standard deviations to the image, edge information at different scales can be extracted [18]. In the multi-scale analysis framework, the result of image $I(x, y)$ smoothed by Gaussian kernel can be expressed as equation (2):

$$L(x, y, \sigma)=G(x, y, \sigma)\cdot I(x, y) \quad (2)$$

Among them, $L(x, y, \sigma)$ represents the image after Gaussian smoothing with a scale of σ, $G(x, y, \sigma)$ represents the Gaussian kernel function, and represents the convolution operation. The Gaussian kernel function is defined as equation (3):

$$G(x, y, \sigma)=\frac{1}{2\pi\sigma^2} e^{-\frac{x^2+y^2}{2\sigma^2}} \quad (3)$$

In this study, a series of different σ values (σ1<σ2<...<σn) were selected to construct a multi-scale space for multi-scale analysis of ruby ball images. A smaller σ value can preserve the detailed information of the image and is suitable for extracting fine edges; A larger value of σ can effectively suppress noise and extract the main structural edges [19].

In order to determine the optimal scale combination, six scale levels were used in the experiment with a range of σ values of [0.5, 2.0] and a step size of 0.3. For each scale σ_i, a corresponding smooth image σ_i is generated. The gradient amplitude $M(x, y, \sigma_i)$ and gradient direction $\theta(x, y, \sigma_i)$ of the image can be calculated using the following formulas (4) and (5):

$$M(x, y, \sigma_i)=\sqrt{\left(\frac{\partial L(x,y,\sigma_i)}{\partial x}\right)^2+\left(\frac{\partial L(x,y,\sigma_i)}{\partial y}\right)^2} \quad (4)$$

$$\theta(x, y, \sigma_i)=\arctan\left(\frac{\partial L(x,y,\sigma_i)/\partial y}{\partial L(x,y,\sigma_i)/\partial x}\right) \quad (5)$$

In practical implementation, in order to improve computational efficiency, a discrete convolution template is used to approximate the gradient calculation. The Sobel operator is applied in the X and Y directions as shown in equations (6) and (7):

$$G_x = \begin{bmatrix} -1 & 0 & 1 \\ -2 & 0 & 2 \\ -1 & 0 & 1 \end{bmatrix} \cdot L(x, y, \sigma_i) \qquad (6)$$

$$G_y = \begin{bmatrix} -1 & -2 & -1 \\ 0 & 0 & 0 \\ 1 & 2 & 1 \end{bmatrix} \cdot L(x, y, \sigma_i) \qquad (7)$$

The key to multi-scale Gaussian kernel smoothing lies in how to effectively fuse edge information at different scales. The weighted fusion strategy based on edge strength is introduced as shown in equation (8):

$$M_{fused}(x, y) = \frac{\sum_{i=1}^{n} w_i \cdot M(x, y, \sigma_i)}{\sum_{i=1}^{n} w_i} \qquad (8)$$

The weight w_i is adaptively determined based on the saliency of the edges at each scale, and the calculation formula is as follows (9):

$$w_i = \frac{E(\sigma_i)}{\sum_{j=1}^{n} E(\sigma_j)} \qquad (9)$$

Among them, $E(\sigma_i)$ represents the edge saliency measure at scale σ_i, which can be determined by indicators such as the average gradient strength of edge points or the number of edge points.

The traditional Canny edge detection algorithm adopts a fixed high and low threshold ratio (usually 2:1), which is difficult to adapt to the complex edge characteristics and lighting changes in ruby ball images. In order to address this issue, this paper proposes an adaptive threshold determination method based on local image characteristics to improve the accuracy and robustness of edge detection [20].

The core idea of adaptive thresholding is to dynamically adjust the threshold based on the local characteristics of the image, so that the threshold value can adapt to the changes in edge intensity in different regions of the image. Firstly, by analyzing the statistical characteristics of image gradient amplitude, a threshold adaptive model is established. The cumulative distribution function (CDF) of the gradient amplitude image $M(x, y)$ is defined as the following equation (10):

$$P(t) = \frac{1}{N} \sum_{(x,y)} \delta(M(x, y) \le t) \qquad (10)$$

Among them, N is the total number of pixels in the image, and $\delta(\cdot)$ is the indicator function. When the condition is met, it takes a value of 1, otherwise it is 0. Based on the cumulative distribution function, the percentage method is used to determine the high and low

thresholds as shown in equations (11) and (12):

$$T_{high}=M_{inv}(P_{high}) \quad (11)$$

$$T_{low}=M_{inv}(P_{low}) \quad (12)$$

Among them, Minv represents the inverse function of the cumulative distribution function, and P_{high} and P_{low} represent the percentages corresponding to high and low thresholds, respectively.

Considering the uneven lighting in the ruby ball image, an adaptive threshold adjustment strategy based on local regions is further introduced. Divide the image into m × n subregions, and calculate the adaptive threshold for each subregion R_{ij} separately using equations (13) and (14):

$$T_{high}(R_{ij})=\mu(R_{ij})+k_{high}\cdot\sigma(R_{ij}) \quad (13)$$

$$T_{low}(R_{ij})=\mu(R_{ij})+k_{low}\cdot\sigma(R_{ij}) \quad (14)$$

Among them, $\mu(R_{ij})$ and $\sigma(R_{ij})$ represent the mean and standard deviation of the gradient amplitude in subregion R_{ij}, respectively. k_{high} and k_{low} are control parameters, and k_{high}=1.5 and k_{low}=0.5 are determined through experiments. In order to avoid sudden changes in threshold values between adjacent regions, bilinear interpolation is used to smooth the threshold distribution as shown in equation (15):

$$T(x,y)=\sum_{i=1}^{m}\sum_{j=1}^{n} w_{ij}(x,y)\cdot T(R_{ij}) \quad (15)$$

Among them, $w_{ij}(x,y)$ is the weight of sub region R_{ij} at position (x,y), determined inversely by the distance from position (x,y) to the center of each sub region.

For the special requirement of edge detection of ruby balls, a global threshold adjustment mechanism based on image entropy is also introduced. The normalized entropy of an image is defined as equation (16):

$$H=-\frac{1}{\log_2(L)}\sum_{i=0}^{L-1} p_i\log_2(p_i) \quad (16)$$

Where L is the grayscale level and p_i is the probability of occurrence of grayscale value i. Based on entropy, adjust the global threshold factor as shown in equation (17):

$$k_{adjust}=k_0\cdot(1+\alpha\cdot(H-H_0)) \quad (17)$$

Among them, k_0 is the benchmark coefficient, H_0 is the reference entropy value, and α is the adjustment amplitude coefficient.

3.2 Secondary Edge Detection: Image Fusion and Multi scale

Enhancement

In high-precision measurement of ruby balls, secondary edge detection is a key step in the entire measurement process. By optimizing and refining the results of primary edge detection, it significantly improves the accuracy of edge localization [21]. This section provides a detailed description of the secondary edge detection algorithm based on multi-scale adaptive edge detection, which integrates the pixel weighted image fusion and multi-scale edge feature enhancement strategies mentioned earlier to form a complete technical solution, as shown in Figure 3.

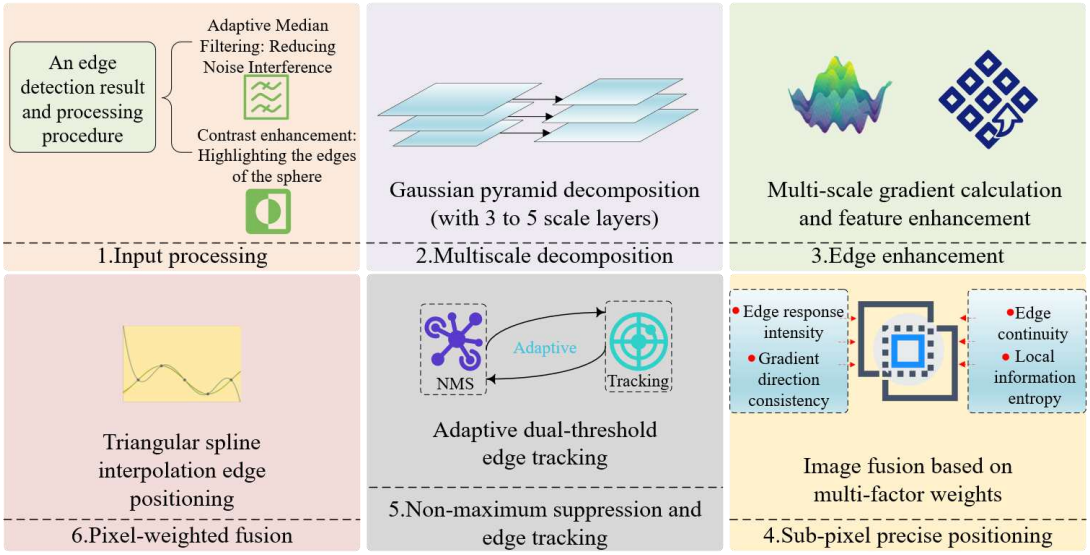


Figure 3 Flow Chart of Secondary Edge Detection Algorithm

In high-precision measurement of ruby balls, the accuracy of edge detection directly affects the accuracy of measurement results. In the actual measurement process, due to factors such as uneven lighting, noise interference, and imaging system distortion, single scale edge detection is often difficult to obtain complete and accurate edge information. In order to address this issue, this paper proposes a multi-scale image fusion method based on pixel weighting, which effectively integrates the advantageous information of edge detection at different scales [22].

The core of pixel weighted image fusion method is to allocate weights based on the reliability of detection results at different scales, in order to generate a more complete and accurate edge image. The specific fusion process is as follows:

Assuming there are n edge images at different scales, represented as {E1, E2,..., En}, the corresponding edge response intensity at pixel point (i, j) is $\{E_1(i,j), E_2(i,j), \ldots, E_n(i,j)\}$. Based on the edge response strength and gradient direction consistency of each pixel, calculate the corresponding weight coefficients $\{w_1(i,j), w_2(i,j), \ldots, w_n(i,j)\}$. The fused edge image $E_{fusion}(i,j)$ can be expressed as the following equation (18):

$$E_{fusion}(i,j)=\sum_{k=1}^{n} w_k(i,j)\cdot E_k(i,j) \qquad (18)$$

The calculation of weight coefficients takes into account two factors: edge response strength and gradient direction consistency. For edge response strength, the weight is directly proportional to the edge strength; For gradient direction consistency, higher weights are assigned when the gradient direction at a certain scale is consistent with the main direction. The weight coefficient can be expressed as the following equation (19):

$$w_k(i,j)=\frac{S_k(i,j)\cdot C_k(i,j)}{\sum_{l=1}^{n} S_l(i,j)\cdot C_l(i,j)} \qquad (19)$$

Among them, $S_k(i,j)$ represents the edge response intensity of pixel point (i,j) at the k-th scale, and $C_k(i,j)$ represents the gradient direction consistency factor of pixel point (i,j) at the k-th scale. This can be obtained by calculating the cosine value of the angle between the gradient direction of this point and the main direction of the local area, as shown in equation (20):

$$C_k(i,j)=\cos\left(\theta_k(i,j)-\theta_{dominant}(i,j)\right) \qquad (20)$$

In order to better handle the continuity features of the edges of ruby balls, this paper further introduced edge continuity weighting factors. For pixels that fall on potential continuous edges, giving higher weights is given by equation (21):

$$w_k'(i,j)=w_k(i,j)\cdot\left(1+\alpha\cdot L_k(i,j)\right) \qquad (21)$$

Among them, $L_k(i,j)$ represents the edge continuity measure of pixel (i,j) at the k-th scale, and α is the adjustment parameter.

In order to suppress the influence of noise and pseudo edges, an adaptive adjustment mechanism based on local information entropy is also introduced, which enables the fusion process to adaptively adjust weight allocation according to local image characteristics. In the edge region of the ruby ball, due to the prominent edge features, its local information entropy is relatively high; In the background region, the local information entropy is relatively low [23]. Based on this characteristic, the revised weight calculation formula is as follows (22):

$$w_k''(i,j)=w_k'(i,j)\cdot\left(1+\beta\cdot H_k(i,j)\right) \quad (22)$$

Among them, $H_k(i,j)$ represents the information entropy of the neighborhood of pixel (i,j) at the k-th scale, and β is the adjustment parameter.

In order to further improve the detection quality of ruby ball edge features, this paper designed a multi-scale edge feature enhancement strategy, which integrates edge information at different scales to enhance real edge features while suppressing noise and false edges. This strategy mainly includes three key steps: multi-scale gradient calculation, edge response fusion, and adaptive threshold determination [24].

The traditional Canny algorithm uses a single scale Gaussian filter for smoothing, which is difficult to simultaneously meet the requirements of noise suppression and edge preservation. This paper uses a multi-scale Gaussian filter to smooth the original image, and then calculates the gradient amplitude and direction at different scales. Multi scale Gaussian filtering can be expressed as equation (23):

$$I_{\sigma_k}(x,y)=I(x,y)*G_{\sigma_k}(x,y) \quad (23)$$

Among them, $I(x,y)$ is the original image, $G_{\sigma_k}(x,y)$ is a Gaussian function with a standard deviation of σ_k, $I_{\sigma_k}(x,y)$ is the image after Gaussian filtering, and * represents the convolution operation. In this study, the selected scale set is $\{\sigma_1, \sigma_2, ..., \sigma_2\}$, where $\sigma_1 < \sigma_2 < ... < \sigma_n$, to cover edge features of different scales.

For each scale σ_k, calculate the corresponding gradient amplitude $M_{\sigma_k}(x,y)$ and gradient direction $\theta_{\sigma_k}(x,y)$ using equations (24) and (25):

$$M_{\sigma_k}(x,y)=\sqrt{\left[I_{\sigma_k}(x+1,y)-I_{\sigma_k}(x-1,y)\right]^2+\left[I_{\sigma_k}(x,y+1)-I_{\sigma_k}(x,y-1)\right]^2} \quad (24)$$

$$\theta_{\sigma_k}(x,y)=\arctan\frac{I_{\sigma_k}(x,y+1)-I_{\sigma_k}(x,y-1)}{I_{\sigma_k}(x+1,y)-I_{\sigma_k}(x-1,y)} \quad (25)$$

After obtaining multi-scale gradient information, it is necessary to effectively fuse edge responses of different scales. Considering the continuity and curvature characteristics of the edge features of ruby balls, this paper designed an edge response fusion method based on gradient consistency and local curvature [25].

Calculate the consistency measure of gradient direction for each pixel at different scales, as shown in equation (26):

$$C(x,y)=\frac{1}{n}\sum_{k=1}^{n}\cos\left(\theta_{\sigma_k}(x,y)-\bar{\theta}(x,y)\right) \quad (26)$$

Among them, $\bar{\theta}(x,y)$ represents the average gradient direction of each scale of the pixel point. The closer the value of $C(x,y)$ is to 1, the more consistent the gradient direction of the point at different scales, and the more likely it is to be a true edge point.

Then, based on gradient consistency and gradient amplitude, the fused edge response strength is calculated using equation (27):

$$M_{fusion}(x,y)=\sum_{k=1}^{n} w_k(x,y)\cdot M_{\sigma_k}(x,y) \quad (27)$$

Among them, $w_k(x,y)$ is the weight coefficient of the kth scale, taking into account two factors: gradient consistency and gradient amplitude, as shown in equation (28):

$$w_k(x,y)=\frac{C_k(x,y)\cdot M_{\sigma_k}(x,y)}{\sum_{j=1}^{n} C_j(x,y)\cdot M_{\sigma_j}(x,y)} \quad (28)$$

$C_k(x,y)$ represents the consistency measure between the gradient direction and the average direction at the k-th scale.

The traditional Canny algorithm uses global high and low thresholds for edge detection, which is difficult to adapt to the characteristic differences of local regions. This paper proposes an adaptive threshold determination method based on local information entropy to address the issue of uneven distribution of edge features of ruby balls.

Calculate the local information entropy distribution of the image using equation (29):

$$H(x,y)=-\sum_{i=0}^{255} p_i(x,y)\log_2 p_i(x,y) \quad (29)$$

Among them, $p_i(x,y)$ represents the probability that the grayscale value in the neighborhood of pixel (x,y) is i.

Then, based on the local information entropy and the fused gradient amplitude, the adaptive high-low threshold is calculated using equations (30) and (31):

$$T_{high}(x,y)=T_{high}^{base}\cdot\left(1-\gamma\cdot\left(H_{max}-H(x,y)\right)\right) \quad (30)$$

$$T_{low}(x,y)=\lambda\cdot T_{high}(x,y) \quad (31)$$

Among them, $T_{high}(x,y)$ is the basic high threshold, usually set as a percentage of the gradient amplitude; H_{max} is the maximum local information entropy in the image; γ is the adjustment parameter that controls the sensitivity of the threshold to local information entropy; λ is the ratio coefficient between the low threshold and the high threshold.

4. Sub pixel localization and circle fitting methods

4.1 Sub pixel positioning

In high-precision measurement of ruby balls, due to the discreteness of image acquisition, the edge positions of the image can often only be represented by pixels, which limits the measurement accuracy. In order to improve the positioning accuracy, sub-pixel edge detection technology is needed to achieve precise positioning of edge positions. As an important sub-pixel localization method, cubic spline interpolation can achieve high-precision edge position calculation while maintaining curve smoothness [26].

The basic idea of cubic spline interpolation is to construct a cubic polynomial function between adjacent data points, so that not only is the interpolation function continuous at each data point, but also the first and second derivatives are continuous, thereby obtaining highly smooth interpolation results. For sub-pixel localization of the edge position of ruby balls, cubic spline interpolation establishes a continuous functional relationship between discrete pixel points to achieve accurate expression of the edge position [27].

Given n+1 data points (x_0,y_0), (x_1,y_1) .., (x_n,y_n), where $x_0 < x_1 < ... < x_n$. Construct n cubic polynomials $S_i(x)$ using cubic spline interpolation, each polynomial applicable to the interval $[x_i, x_{i+1}]$, satisfying the following condition as equation (32):

$$S_i(x)=a_i+b_i(x-x_i)+c_i(x-x_i)^2+d_i(x-x_i)^3,i=0,1,,n-1 \quad (32)$$

Among them, a_i, b_i, c_i, and d_i are undetermined coefficients. In order to ensure the smoothness of the interpolation function, the following conditions must be met:

Interpolation condition: $S_i(x_i) = y_i$ and $S_i(x_{i+1})=y_{i+1}$

The first derivative is continuous: $S'_i(x_{i+1})=y'_{i+1}$, where i = 0,1, ..., n-2

Second derivative continuous: $S''_i(x_{i+1})=y''_{i+1}$, where i=0,1,..., n-2

In order to construct a complete interpolation system, it is also necessary to specify boundary conditions, commonly including natural boundary conditions (where the second derivative is zero at the endpoints) and periodic boundary conditions. In ruby ball edge detection, natural boundary conditions are usually used as shown in equation (33):

$$S''_0(x_0)=0,S''_{n-1}(x_n)=0 \quad (33)$$

Solving the above equation system can obtain all undetermined coefficients, thus constructing a complete cubic spline interpolation function. For the edge gradient image of

ruby balls, cubic spline interpolation can not only smoothly interpolate the discrete gradient values, but also accurately locate the gradient extremum points, that is, the precise positions of the edges [28].

In ruby ball edge detection, single scale edge detection often cannot adapt to various interference factors in complex environments, such as noise, lighting changes, etc. The multi-scale feature weight fusion method extracts edge features at different scales and assigns weights based on the reliability of the features, achieving effective integration of edge information and greatly improving the accuracy and robustness of edge detection [29].

The core idea of multi-scale feature weight fusion is to utilize the complementarity of edge features at different scales to weight and combine edge information. In ruby ball image processing, Gaussian smoothing is first applied to the image at multiple scales to form a scale space sequence as shown in equation (34):

$$L(x, y, \sigma_i)=G(x, y, \sigma_i)*I(x, y) \quad (34)$$

Among them, $I(x, y)$ represents the original image, $G(x, y, \sigma_i)$ represents the Gaussian function with a standard deviation of σ_i, * represents the convolution operation, and $L(x, y, \sigma_i)$ represents the smoothed image with a scale of σ_i.

For each scale of smooth images, the gradient amplitude and direction are calculated using equations (35) and (36):

$$M_i(x, y)=\sqrt{\left(\frac{\partial L_i}{\partial x}\right)^2+\left(\frac{\partial L_i}{\partial y}\right)^2} \quad (35)$$

$$\theta_i(x, y)=\arctan\left(\frac{\partial L_i}{\partial y}/\frac{\partial L_i}{\partial x}\right) \quad (36)$$

Among them, $M_i(x, y)$ and $\theta_i(x, y)$ respectively represent the gradient amplitude and gradient direction at scale σ_i.

Weight allocation is a crucial step in multi-scale fusion. Based on the stability and consistency of gradient amplitude, the weight function is designed as the following equation (37):

$$w_i(x, y)=\frac{\lambda_i \cdot M_i(x,y) \cdot C_i(x,y)}{\sum_{j=1}^{n} \lambda_j \cdot M_j(x,y) \cdot C_j(x,y)} \quad (37)$$

Among them, λ_i is a preset scale weight coefficient that can be adjusted according to the importance of different scales; $C_i(x, y)$ is a consistency measure, which represents the degree of consistency between the edge direction at the current scale and adjacent scales, and can be

expressed as equation (38):

$$C_i(x,y)=\frac{1}{n-1}\sum_{j=1,jeqi}^{n}\cos\left(2\left(\theta_i(x,y)-\theta_j(x,y)\right)\right) \quad (38)$$

By using the above weight functions, adaptive fusion of features at different scales has been achieved, and the weighted fusion gradient amplitude and direction are obtained as equations (39) and (40):

$$M_{fused}(x,y)=\sum_{i=1}^{n} w_i(x,y)\cdot M_i(x,y) \quad (39)$$

$$\theta_{fused}(x,y)=\arg\left\{\sum_{i=1}^{n} w_i(x,y)\cdot e^{j\theta_i(x,y)}\right\} \quad (40)$$

4.2 Circle fitting and diameter calculation

In the high-precision measurement process of ruby balls, after completing sub-pixel positioning of edge points, it is necessary to use the circle fitting algorithm to fit these edge points into a standard circle to obtain the accurate diameter of the ruby ball. This paper adopts an improved least squares circle fitting method based on the principle of geometric distance minimization, which can effectively eliminate random errors in edge extraction and improve overall fitting accuracy [30].

The algebraic distance least squares circle fitting method is simple to calculate, but its geometric meaning is not clear, which can easily introduce system bias. The geometric distance least squares method directly optimizes the Euclidean distance between points and circles, which has better geometric interpretability and fitting accuracy. Let the equation for a circle be the following equation (41):

$$(x-a)^2+(y-b)^2=r^2 \quad (41)$$

Among them, (a, b) are the center coordinates, and r is the radius of the circle. For any edge point (x_i, y_i), its geometric distance to the circle is given by equation (42):

$$d_i=\left|r-\sqrt{(x_i-a)^2+\left(y_i-b\right)^2}\right| \quad (42)$$

The objective function based on geometric distance minimization can be expressed as the following equation (43):

$$F(a,b,r)=\sum_{i=1}^{n} d_i^2=\sum_{i=1}^{n}\left[r-\sqrt{(x_i-a)^2+\left(y_i-b\right)^2}\right]^2 \quad (43)$$

In order to find the optimal circular parameters, it is necessary to take the derivative of the

objective function F (a, b, r) and make it equal to zero, as shown in equation (44):

$$\frac{\partial F}{\partial a}=\frac{\partial F}{\partial b}=\frac{\partial F}{\partial r}=0 \qquad (44)$$

This type of nonlinear optimization problem is difficult to solve directly. This paper adopts an iterative optimization strategy and combines it with the Levenberg Marquardt algorithm to achieve parameter convergence. The algorithm process is as follows:

Obtain initial circle parameter estimates (a_0, b_0, r_0) through algebraic methods. The algebraic method is based on expanding the circular equation as shown in equation (45):

$$(x-a)^2+(y-b)^2=r^2 \Rightarrow x^2+y^2-2ax-2by+a^2+b^2-r^2=0 \qquad (44)$$

Let $c=a^2+b^2-r^2$, $d=-2a$, $e=-2b$, and rewrite the circle equation as follows (45):

$$x^2+y^2+dx+ey+c=0 \qquad (45)$$

The parameters c, d, and e can be solved using the least squares method, and the initial circle parameters can be obtained as shown in equation (46):

$$a_0=-\frac{d}{2}, b_0=-\frac{e}{2}, r_0=\sqrt{a_0^2+b_0^2-c} \qquad (46)$$

Subsequently, the Levenberg Marquardt algorithm was used for iterative optimization. In each iteration, calculate the Jacobian matrix J as shown in equation (47):

$$J_i=\left[\frac{\partial d_i}{\partial a} \quad \frac{\partial d_i}{\partial b} \quad \frac{\partial d_i}{\partial r}\right] \qquad (47)$$

The partial derivatives are given by the following equations (48), (49), and (50):

$$\frac{\partial d_i}{\partial a}=\frac{(x_i-a)}{\sqrt{(x_i-a)^2+(y_i-b)^2}} \qquad (48)$$

$$\frac{\partial d_i}{\partial b}=\frac{y_i-b}{\sqrt{(x_i-a)^2+(y_i-b)^2}} \qquad (49)$$

$$\frac{\partial d_i}{\partial r}=-1 \qquad (50)$$

The parameter update formula is as follows (51):

$$\begin{bmatrix}\Delta a\\ \Delta b\\ \Delta r\end{bmatrix}=\left(J^TJ+\lambda I\right)^{-1}J^Td \qquad (51)$$

Among them, λ is the damping factor, which is dynamically adjusted according to the convergence of each iteration. When the parameter change is less than the preset threshold, the iteration ends.

This paper has improved the traditional Levenberg Marquardt algorithm by introducing an edge point filtering mechanism based on RANSAC, which can effectively reduce the impact

of outliers on the fitting results. The pseudocode can be found in Algorithm 1.

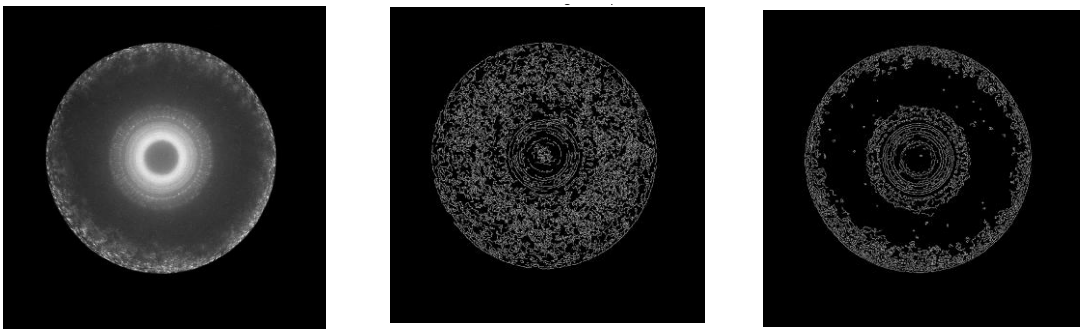
Algorithm 1 Levenberg-Marquardt Optimization

Initialize parameters θ_0, damping factor λ, and tolerance ϵ
Compute initial residual r_0 and Jacobian J_0
while $|r_k - r_{k-1}| > \epsilon$ **do**
    Compute update step $\Delta\theta = -(J_k^T J_k + \lambda I)^{-1} J_k^T r_k$
    Update parameters $\theta_{k+1} = \theta_k + \Delta\theta$
    Compute new residual r_{k+1} and Jacobian J_{k+1}
    if $|r_{k+1}| < |r_k|$ **then**
        Decrease damping factor $\lambda = \lambda/2$
    else
        Increase damping factor $\lambda = 2\lambda$
        Revert to previous parameters $\theta_{k+1} = \theta_k$
    end if
    $k = k + 1$
end while
return θ_k

Algorithm 1 Pseudo code of Levenberg Marquardt Optimization

5. Algorithm comparison and performance verification

5.1 Comparison with traditional measurement methods



(a) Ruby Ball Original Image

(b) Edge detection under Canny operator

(c) Improved edge detection under Canny operator

Figure 4 Original Image and Primary Edge Image of Ruby Ball

Figure 4 shows the comparison between the original image of the ruby ball dark field and different edge detection algorithms. Figure 4 (a) shows the original image of the ruby sphere, which exhibits high reflectivity and distinct circular diffraction texture in its edge region. The overall contrast is low, which increases the difficulty of edge extraction. Figure 4 (b) shows the edge detection result under the traditional Canny operator. Although it can extract some circular structures and texture information, the image has dense noise points, many edge fractures, and false contours, resulting in insufficient extraction accuracy and continuity.

Figure 4 (c) shows the edge detection results under the improved Canny operator, which uses multi-scale Gaussian smoothing and adaptive thresholding methods to effectively suppress background noise interference, enhance edge response, significantly improve the continuity and clarity of edge extraction, and more accurately preserve the true contour and structural features of ruby balls. This verifies the superiority of the improved algorithm in high reflection and edge blurred target measurement.

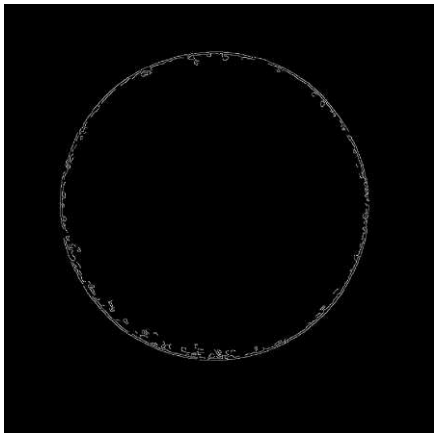


Figure 5 Ideal edge of ruby sphere extracted by secondary edge detection

Figure 5 shows the effect of the ruby ball after secondary edge detection. It is evident that compared to primary edge detection, the continuity and integrity of the edges have been significantly improved. The pseudo edges caused by imaging noise and internal interference loops have been basically suppressed, and the contour lines are clear, fine, and well closed, only retaining the true boundary of the outermost layer of the ruby ball. This lays a stable foundation for subsequent sub-pixel fitting and high-precision size measurement, fully reflecting the superiority of multi-scale edge enhancement and local adaptive thresholding methods in complex object detection.

In order to comprehensively evaluate the performance differences between the multi-scale adaptive edge detection method proposed by this paper and traditional methods, this section systematically compares and analyzes the three methods. Under the same experimental conditions, three methods were used to measure a standard size of 5.000mm ruby ball sample, and comparisons were made from multiple dimensions such as measurement accuracy, noise resistance, computational efficiency, and adaptability. The results are shown in Table 1.

Table 1 Comparison of Three Methods for Measuring the Performance of Ruby Balls

Performance index	Proposed method	Hessian Matrix Method	Regionprops method
Average measurement value（mm）	5.0016	5.0047	5.0092
Mean absolute error（μm）	1.6	4.7	9.2
Average relative error（%）	0.032	0.094	0.184
Standard deviation of measured values（μm）	0.7	1.3	2.3
Average processing time（ms）	215.3	289.5	140.5
SNR=20dB time error（μm）	2.4	6.5	11.8
SNR=15dB time error（μm）	3.8	9.3	15.6

According to Table 1, in terms of measurement accuracy, the multi-scale adaptive edge detection method proposed by this paper performs the best, with an average absolute error of only 1.6μm, which is about 66% lower than the Hessian matrix method and about 83% lower than the regionprops method. The standard deviation is 0.7μm, demonstrating excellent repeatability and stability. The improvement in accuracy is mainly due to the fusion of multi-scale edge information, sub-pixel localization, and improved least squares circle fitting algorithm. The anti noise performance test shows that when the signal-to-noise ratio (SNR) drops to 20 dB, the error of this method only increases to 2.4μm, while the Hessian matrix and regionprops methods increase to 6.5μm and 11.8μm, respectively; When the SNR decreases to 15dB, the errors of the three methods are 3.8μm, 9.3μm, and 15.6μm, respectively, further demonstrating the stability of the method in noisy environments.

In terms of computational efficiency, the regionprops method is the fastest (140.5 ms), with a speed of 215.3 ms, which is about 26% faster than the Hessian matrix method (289.5 ms). While significantly improving accuracy, it still meets the real-time requirements of practical applications. In terms of adaptability, the regionprops method is sensitive to lighting uniformity, the Hessian matrix method is sensitive to high-frequency noise, and this method

has stronger lighting and noise adaptability through multi-scale fusion and adaptive threshold strategy. In terms of parameter settings, regionprops is the simplest and the complexity of this method is moderate, while the Hessian matrix method is the most complex.

5.2 Measurement experiments for components of different sizes

In order to comprehensively evaluate the measurement accuracy and adaptability of the proposed multi-scale adaptive edge detection algorithm on components of different sizes, this paper selected ruby balls and ceramic balls of different diameter specifications as measurement objects. All samples have a nominal accuracy level of G5, a sphericity error of $\leqslant$0.5μm, a surface roughness Ra between 0.012-0.022μm, and a hardness of 2300 HV for ruby and 1800 HV for ceramic. The experiment was conducted in an environment of 23±0.5℃ and 50±5% RH using a high-resolution camera with a resolution of 4096×3000 pixels for dark field imaging, with a pixel equivalent of approximately 1.68μm/pixel. Each sample is subjected to 10 repeated measurements, and the mean and standard deviation are recorded. The results are shown in Figure 6. The CMM measurement value of the smallest sample R-3.0 (3mm ruby ball) is 3.0012mm, and the measurement value of the largest sample C-12.0 (12mm ceramic ball) is 12.0006mm. During the measurement, it was found that the ruby ball has slightly lower edge contrast due to its semi transparent nature, especially when the diameter is 3-5 mm, which requires higher imaging requirements; Ceramic balls are prone to weak noise at high resolution and need to be suppressed through algorithms. When measuring samples of different sizes, the system adjusts the magnification and field of view according to the size, and completes calibration before measurement to ensure accuracy. The industry standard requires that the measurement error of a 5mm sphere should be controlled within 0.5μm. The average absolute error of this paper's measurement results is lower than the standard, which verifies the high accuracy and good adaptability of the algorithm under complex conditions.

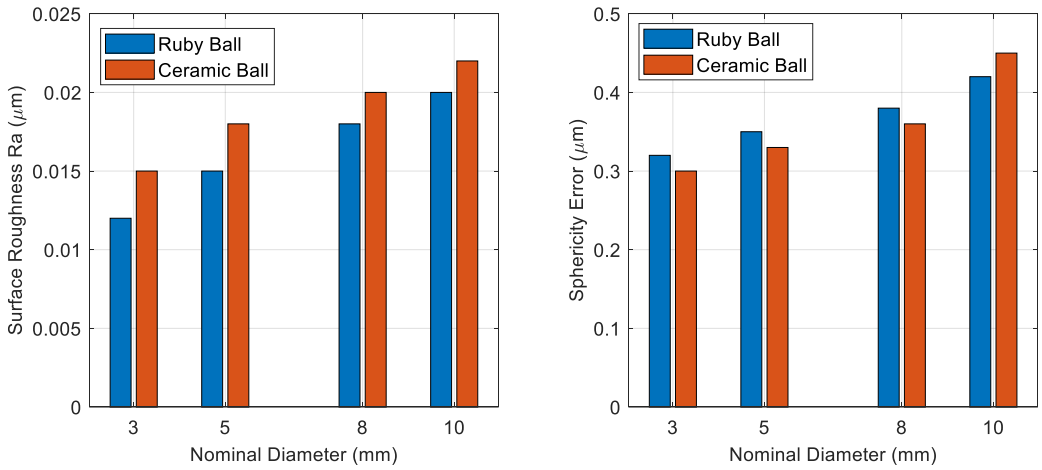


Figure 6 Comparison of sample parameters between ruby balls of different diameters and ceramic balls

Based on the experiments of ruby balls (R-3; R-5; R-8) and ceramic balls (C-3; C-5; C-8), this paper further extended the measurement range to hard alloy balls (H-3; H-5; H-8) to verify the applicability of the proposed multi-scale adaptive edge detection algorithm in precision balls of different materials and sizes (see Figure 7). The results showed that the measurement errors of the three types of samples remained within the range of 0.2-0.3μm, with repeatability (1σ) better than 0.15μm, significantly better than the improved Hough transform method (error 0.5-0.9μm) and the traditional Canny algorithm (error 1.1-1.8μm). Among them, hard alloy balls have more stable surface reflection characteristics and slightly better measurement repeatability, ranging from 0.09-0.12μm, while ruby balls have slightly lower repeatability due to their semi transparent properties.

Further comparison of samples with different diameters (3-9mm) shows that size has little effect on measurement accuracy, and all diameters can achieve micrometer level measurement errors. In addition, under interference conditions such as ± 15% light fluctuation, 0.05mm vibration, and a 5dB reduction in signal-to-noise ratio, the algorithm error amplification does not exceed 0.2μm, still meeting the requirements of high-end manufacturing for measurement stability and anti-interference. Overall, the proposed algorithm performs outstandingly in terms of generality, accuracy, and environmental adaptability, and can provide a highly reliable solution for non-contact measurement of precision spheres of different materials.

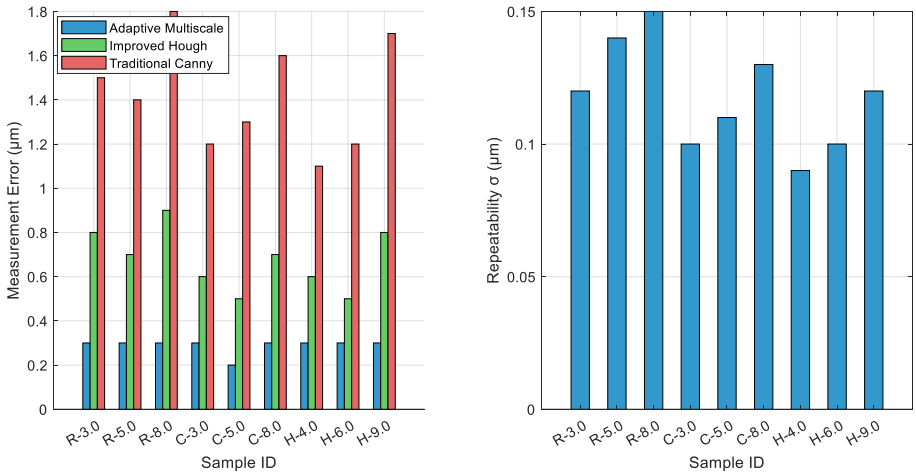


Figure 7 Measurement results and error analysis of three types of material components

5.3 Robustness analysis under different noise conditions

In industrial environments, the measurement of ruby balls is inevitably affected by Gaussian noise interference. In order to verify the robustness of the multi-scale adaptive edge detection algorithm, this paper simulated Gaussian noise of different intensities (σ=0.01 to 0.09) on standard test images and compared it with traditional Canny algorithm and Hessian matrix method .

The experimental results are shown in Figure 8. As the noise intensity increases, the measurement errors of the three algorithms all increase, but this algorithm has the best noise resistance performance: At σ=0.09, the measurement error is only 1.37 ± 0.21μm, while the traditional Canny algorithm reaches 3.48 ± 0.57μm, and the Hessian matrix method is 2.63 ± 0.43μm, both significantly higher than this method. Overall, the algorithm showed an error increase of only 0.75μm during the noise growth process from 0.01 to 0.09, which is about 1.8μm and 1μm less than the traditional Canny algorithm and Hessian matrix method, respectively. This demonstrates a smoother error growth curve and better robustness. In addition, the edge detection results show that the traditional Canny algorithm generates a large number of pseudo edges under high noise, while the multi-scale adaptive algorithm can effectively maintain edge continuity and localization accuracy, verifying its application value in complex industrial conditions.

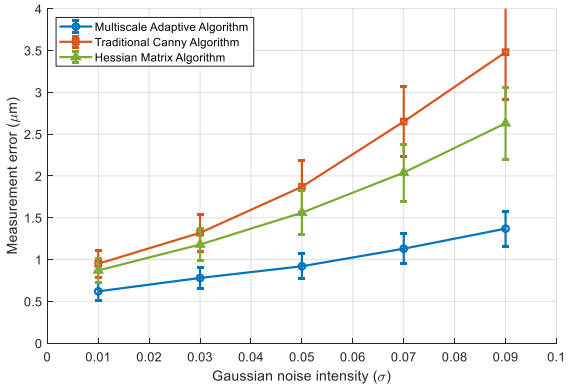


Figure 8 Comparison of measurement errors of various algorithms under different levels of Gaussian noise

In order to verify the robustness of the proposed multi-scale adaptive edge detection algorithm under different imaging conditions, this paper conducted a systematic comparative experiment. The camera gain was set separately in the experiment to measure the ruby ball image, and the results are shown in Figure 9-10.

As the gain increases, the edge localization errors of all three algorithms increase, but the multi-scale adaptive algorithm consistently outperforms the control method significantly, as shown in Figure 9. Under high gain conditions of 20 dB, the positioning error of this algorithm (0.132 ± 0.022 pixels) is about 55% lower than the traditional Canny algorithm and about 43% lower than the Hessian matrix method, demonstrating good noise resistance performance.

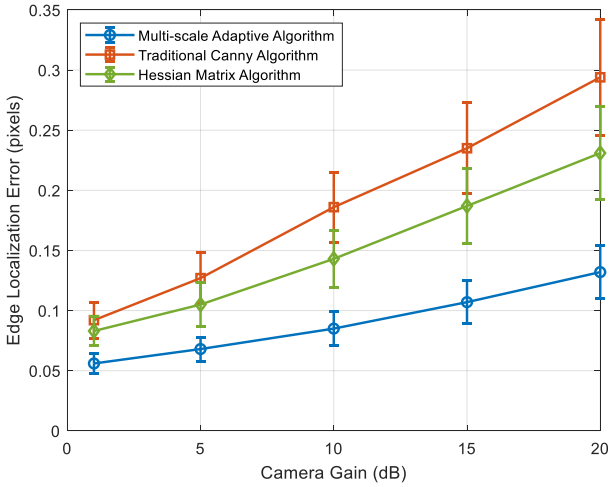


Figure 9 Edge localization errors of various algorithms under different camera gains

Improving the signal-to-noise ratio can effectively reduce measurement errors, but traditional algorithms show significant performance degradation at low signal-to-noise ratios (15 dB), with measurement errors reaching 3.26 ± 0.54μm (Canny) and 2.57 ± 0.42μm (Hessian), respectively, while multi-scale adaptive algorithms only achieve 1.43 ± 0.24μm. Even under high signal-to-noise ratio (35 dB) conditions, the measurement error of this algorithm (0.59 ± 0.09μm) is still significantly lower than traditional methods, fully demonstrating its stability and reliability under different imaging conditions, as shown in Figure 10.

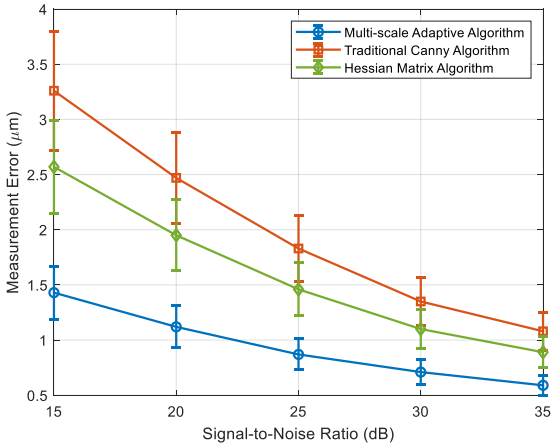


Figure 10 Measurement errors of various algorithms under different signal-to-noise ratio conditions

From the above comparison, it can be seen that the multi-scale adaptive edge detection algorithm exhibits excellent adaptability and robustness under changes in gain and signal-to-noise ratio, meeting the practical needs of industrial high-precision measurement.

6. Conclusion

This paper studied a high-precision non-contact measurement method for ruby balls based on multi-scale adaptive edge detection, which comprehensively improved the performance of edge detection and diameter calculation. Experiments have shown that on a standard 5mm ruby ball sample, the average absolute measurement error of this algorithm is 1.6μm, significantly lower than the Hessian matrix method (4.7μm) and regionprops method (9.2μm), with a standard deviation of only 0.7μm, demonstrating excellent repeatability. Under the

condition of reducing the signal-to-noise ratio from 35 dB to 15 dB, the increase in measurement error is only about 0.8μm, which has significant advantages compared to the traditional Canny algorithm (error amplification of 2.2μm). For different materials (ruby, ceramic, hard alloy) and spherical samples of different sizes (3-12mm), the measurement error of this method is stable at 0.2-0.3μm, and the repeatability is better than 0.15μm. When the camera gain is increased to 20 dB, the edge localization error of this algorithm is controlled at 0.132±0.022 pixels, which is about 55% lower than the traditional Canny algorithm, indicating its excellent robustness under noise conditions. Overall, this method has high precision, strong adaptability, and good anti-interference performance, fully meeting the needs of micrometer level measurement in industrial environments, and providing an effective and reliable technical means for non-contact measurement of high-end precision components.

Reference

[1] Guoyin Shen, Jesse S. Smith, Curtis Kenney Benson & Yanbin Wang. (2025). Calibration of ruby's luminescence shift from the bismuth I-II transition: constraints on the initial slope of ruby gauge. High Pressure Research, 45 (1), 17-28.

[2] Borong Wu, Chuang Zeng & Qiaolin Li. (2024). Comparison Analysis of Roundness Measurement of Small Cylindrical Workpieces with Different Styluses.. Sensors (Basel, Switzerland), 24 (12), 3819-3819.

[3] Oertel Erik & Manske Eberhard. (2024). Influence of the reference surface and AFM tip on the radius and roundness measurement of micro spheres. Measurement Science and Technology, 35 (2),

[4] Borkenstein Andreas F, Borkenstein EvaMaria, Mühlbacher Inge & Flock Michaela. (2023). Nano-Indentation to Determine Mechanical Properties of Intraocular Lenses: Evaluating Penetration Depth, Material Stiffness, and Elastic Moduli.. Ophthalmology and therapy, 12 (4), 2087-2101.

[5] Yan Jinwei,Liu Xiaodi,Gorelli Federico Aiace,Xu Haian,Zhang Huichao,Hu Huixin... & DalladaySimpson Philip. (2022). Compression rate of dynamic diamond anvil cells from room temperature to 10 K.. The Review of scientific instruments, 93 (6), 063901-063901.

[6] Renner Ilse E, Gardner Gary & Fritz Vincent A. (2021). Manipulation of Continuous and

End-of-Day Red/Far-Red Light Ratios Affects Glucobrassicin and Gluconasturtiin Accumulation in Cabbage (Brassica oleracea) and Watercress (Nasturtium officinale), Respectively.. Journal of agricultural and food chemistry, 69 (47),

[7] Linsler Dominic, Ruebeling Friederike & Greiner Christian. (2021). Subsurface Microstructural Evolution during Scratch Testing on Bcc Iron. Metals, 11 (8), 1258-1258.

[8] Oertel Erik & Manske Eberhard. (2021). Radius and roundness measurement of micro spheres based on a set of AFM surface scans. Measurement Science and Technology, 32 (4), 044005-.

[9] Anonymous. (2021). Sapphire and ruby balls. Laser Focus World, 57 (1), 58-.

[10] Galeva H., Uzunov T., Stoev Y., Sofronov Y. & Todorov G.. (2021). Investigation of the deviation during the information transfer from the prosthetic field to the laboratory scanners. IOP Conference Series: Materials Science and Engineering, 1056 (1), 012010-.

[11] Helena Checa, Giulia Margaritelli, Leopoldo D Pena, Jaime Frigola, Isabel Cacho, Roberto Rettori & Fabrizio Lirer. (2020). High resolution paleo-environmental changes during the Sapropel 1 in the North Ionian Sea, central Mediterranean. The Holocene, 30 (11), 095968362094109.

[12] Chuanzhi Fang,Qiangxian Huang,Xuemeng Ding,Rongjun Cheng,Liansheng Zhang,Chaoqun Wang... & Hongli Li. (2020). Measurement and uncertainty evaluation of the microsphere used for micro-CMM probe. Measurement Science and Technology, 31 (2), 025004-025004.

[13] Mayuri Kerr, Neil Park, David Leeson & Sergey Nikolskiy. (2019). Dimensional accuracy of microcomputed tomography-scanned half-arch impressions. The Journal of Prosthetic Dentistry, 121 (5), 797-802.

[14] Riyadh M Alzahrani,Mohamed Yacin Sikkandar,S Sabarunisha Begum,Ahmed Farag Salem Babetat,Maryam Alhashim,Abdulrahman Alduraywish... & Eddie Y K Ng. (2025). Early breast cancer detection via infrared thermography using a CNN enhanced with particle swarm optimization.. Scientific reports, 15 (1), 25290.

[15] Shaomiao Chen, Ao Bai, Zhiwen Lei, Liming Jiang, Dacheng He, Kuanching Li & Wei Liang. (2025). An Adaptive Differentiable Neural Network Architecture Search Algorithm and Its Application for sewer defect detection. Telecommunication Systems, 88 (3), 101-101.

[16] Baoyu Wang, Mao Yang, Pingping Cao, Aihong Shen & Yan Liu. (2025). STNet: a lightweight spectral transform framework for salient object detection. Complex & Intelligent Systems, 11 (9), 381-381.

[17] Boao Gong, Haoran Zhang, Bohan Ma & Zhiyong Tao. (2025). Enhancing real-time low-light object detection via multi-scale edge and illumination-guided features in YOLOv8. The Journal of Supercomputing, 81 (10), 1120-1120.

[18] Shen Guo, Ying Li, Jiashuo Shang & Lingxiao Cheng. (2025). GSSNet: Gated selective scan network for port oil spill pollution detection. Measurement, 256 (PB), 118086-118086.

[19] Gerardo Antonio Hernández Torres & Eddy Sánchez DelaCruz. (2025). Challenges and opportunities of ambient intelligence (AmI) in the 21st century: a historical review. Evolutionary Intelligence, 18 (4), 80-80.

[20] Morten Sielnik Andersen, Jens Christian Pedersen, Bjarke Jørgensen, Mogens Hinge & René Lynge Eriksen. (2025). Modular calibration board for automated calibration of hyperspectral cameras.. Spectrochimica acta. Part A, Molecular and biomolecular spectroscopy, 344 (Pt 1), 126608.

[21] Haili Wang, Muye Zhang, Linghao Zhang, Xiaoxiao Zhu & Qixin Cao. (2025). Real-Time Hand Gesture Recognition in Clinical Settings: A Low-Power FMCW Radar Integrated Sensor System with Multiple Feature Fusion. Sensors, 25 (13), 4169-4169.

[22] Yonghu Chang, Changwen Pu, Shijie Li & Yongchuan Tang. (2025). An improved YOLOv7-Tiny method for liquid level detection in medical infusion monitoring.. Computers in biology and medicine, 196 (Pt A), 110656.

[23] Fatima Asiri, Wajdan Al Malwi, Fahad Masood, Mohammed S. Alshehri, Tamara Zhukabayeva, Syed Aziz Shah & Jawad Ahmad. (2025). Privacy Preserving Federated Anomaly Detection in IoT Edge Computing Using Bayesian Game Reinforcement Learning. Computers, Materials & Continua, 84 (2), 3943-3960.

[24] Boyu Feng, Bo Liu, Li Song, Yongyan Chen, Xiaofeng Jiao & Baiqiang Wang. (2025). A novel edge crop method and enhanced YOLOv5 for efficient wind turbine blade damage detection. Scientific Reports, 15 (1), 22777-22777.

[25] Yu Lin, Shuiyuan He & Weidong Luo. (2025). Dynamic margin contrastive learning for open-set recognition in long-tailed sonar imagery. Scientific Reports, 15 (1), 22617-22617.

[26] Hafiz Gulfam Ahmad Umar, Iqra Yasmeen, Muhammad Aoun, Tehseen Mazhar, Muhammad Amir Khan, Ines Hilali Jaghdam & Habib Hamam. (2025). Energy-efficient deep learning-based intrusion detection system for edge computing: a novel DNN-KDQ model. Journal of Cloud Computing, 14 (1), 32-32.

[27] Bakhita Salman, Andres Lopez & Nathanielle Delapena. (2025). Breaking language barriers with image detection and natural language processing model for English to Spanish translation. Discover Applied Sciences, 7 (7), 682-682.

[28] Meiqi Zhong, Linjing Wei & Henghui Mo. (2025). YOLOv8n-DSDL: A lightweight dual-backbone network with decoupled self-attention for cotton maturity detection. Journal of King Saud University Computer and Information Sciences, 37 (5), 88-88.

[29] G. Gomez Proto, E. Mancin, A. Quaglia, F. Sbarra, R. Mantovani & C. Sartori. (2025). Exploring genetic diversity and genomic inbreeding across local beef cattle breeds. animal, 19 (7), 101565-101565.

[30] Saeed Ullah, Junsheng Wu, Mian Muhammad Kamal & Abdul Khader Jilani Saudagar. (2025). KronNet a lightweight Kronecker enhanced feed forward neural network for efficient IoT intrusion detection. Scientific Reports, 15 (1), 20850-20850.